ARTICLE

Check for updates

Few-femtosecond phase-sensitive detection of infrared electric fields with a third-order nonlinearity

Hannes Kempf [1], Philipp Sulzer [1], Andreas Liehl[1], Alfred Leitenstorfer [1] & Ron Tenne [1✉]

Measuring an electric field waveform beyond radio frequencies is often accomplished via a second-order nonlinear interaction with a laser pulse shorter than half of the field's oscillation period. However, synthesizing such a gate pulse is extremely challenging when sampling mid- (MIR) and near- (NIR) infrared transients. Here, we demonstrate an alternative approach: a third-order nonlinear interaction with a relatively long multi-cycle pulse directly retrieves an electric-field transient whose central frequency is 156 THz. A theoretical model, exploring the different nonlinear frequency mixing processes, accurately reproduces our results. Furthermore, we demonstrate a measurement of the real part of a sample's dielectric function, information that is challenging to retrieve in time-resolved spectroscopy and is therefore often overlooked. Our method paves the way towards experimentally simple MIR-to-NIR time-resolved spectroscopy that simultaneously extracts the spectral amplitude and phase information, an important extension of optical pump-probe spectroscopy of, e.g., molecular vibrations and fundamental excitations in condensed-matter physics.

[1] Department of Physics and Center for Applied Photonics, University of Konstanz, Konstanz, Germany. ✉email: ron.tenne@uni-konstanz.de

In optical spectroscopy, the frequency-resolved amplitude and phase of light waves encode valuable information about the probed sample. Nonetheless, in time-resolved spectroscopy, a prominent tool for biological, chemical, and condensed-matter research, the phase information is not commonly obtained[1,2]. This results mainly from the practical difficulty in measuring phase with linear interferometric techniques over a broad spectral band and a large range of time delays[1,3,4]. Phase information is even of greater significance to resolve the electric field of an optical pulse in the time domain. While for radio-frequency signals an oscilloscope readily performs this task, the equivalent 'optical oscilloscope' still lacks a general solution and is therefore the goal of current research[5,6]. Extending phase-sensitive measurements to the mid-infrared (MIR) often presents an additional obstacle, the lack of high-sensitivity and low-noise detectors[7,8].

In the few-terahertz (THz) regime, nonlinear techniques offer an alternative approach that circumvents both of these issues[9,10]. For example, in electro-optic sampling (EOS), nonlinear interaction with a probe pulse, shorter than the half-cycle period of the signal, temporally samples the electric field[11,12]. Moreover, the phase information is transferred from the inconvenient-to-detect THz and multi-THz ranges to the NIR or visible spectral bands where low-noise sensors and arrays are readily available[13,14].

Recently, these considerations motivated a growing interest in the expansion of nonlinear phase-detection methods to the MIR and NIR[5,10,15–19]. This progress supports the ongoing scientific effort in controlling solid-state systems on a few-femtosecond time scale with precisely characterized ultrashort laser pulses[20–24]. Moreover, the addition of spectral phase information promises to expand the capabilities of existing MIR and NIR spectroscopy and imaging techniques[25]. However, extending EOS to field transients in the MIR and NIR requires the stable generation of probe pulses with a few-femtosecond duration, an extremely challenging experimental task. An alternative successful strategy that circumvents this requirement is to exploit a highly nonlinear interaction between a strong probe pulse and the signal field[5,17,18,26,27]. The high degree of nonlinearity results in a large amplification of the output at the temporal peak of the probe field, effectively creating a gating window shorter than half of the signal's period[17]. Nevertheless, this strategy requires the generation of ultrashort few-cycle probe pulses. The necessity of very stable pulses in conjunction with a high peak field poses an additional experimental hurdle. More recently, a single-shot waveform measurement harnessing third-order nonlinearity has been demonstrated[28]. This implementation relied on μJ-scale pulse energies, typically limiting its application to laser amplifiers with kHz pulse repetition rates. Altogether, a simplified and general scheme to directly measure the spectral amplitude and phase of electric-field transients in the MIR and NIR is an ongoing challenge of high significance.

In this work, we introduce a method that strives to meet this challenge—multi-cycle third-order sampling (MCTOS). Surprisingly, a phase-sensitive measurement is achieved using third-order nonlinear interactions alone, thus, without generating a sub-cycle gating duration or a carrier-envelope-phase (CEP)-stable signal pulse. The low-order nonlinear signal is realized with sub-nanojoule pulses and can be accurately described with a straightforward perturbative model. Therefore, MCTOS represents a convenient scheme for both pulse characterization and time-resolved phase sensing in the attractive MIR and NIR spectral windows.

Results and discussion

Experimental implementation. In the following, we provide a concise description of the experimental setup; further details can
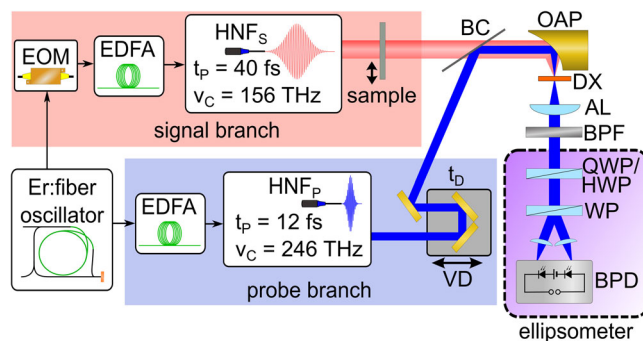

Fig. 1 Scheme of the experimental setup. The signal and probe pulses are generated in two distinct highly nonlinear fibers (HNF$_S$ and HNF$_P$). The third-order nonlinear interaction occurs in the detection crystal (DX; Si or GaSe) and the induced polarization change is analyzed by an ellipsometer. EOM electro-optic modulator, EDFA erbium-doped fiber amplifier, VD variable optical delay stage, BC beam combiner (500 μm thick Si wafer), OAP off-axis parabolic mirror, AL achromatic lens, BPF bandpass filter, QWP/HWP quarter- or half-wave plate, WP Wollaston prism, BPD: balanced photodiodes.

be found in the Methods section. Figure 1 depicts the schematic setup of MCTOS. The pulsed output of a mode-locked Er:fiber laser oscillator with a 40 MHz repetition rate and center frequency of 193 THz (wavelength of 1550 nm) is separated into two branches to generate the signal and probe pulses. A fiber-coupled electro-optic modulator (EOM) reduces the repetition rate in the signal branch to 20 MHz. Thanks to the strong mode confinement within a highly nonlinear fiber (HNF), the telecom pulse undergoes efficient third-order nonlinear interaction generating spectral components within the range from 130 to 350 THz[29]. This mechanism is applied to synthesize both the signal and the probe pulse in two distinct HNFs. The signal branch features a center frequency of 156 THz (wavelength of 1.92 μm), 1 nJ pulse energy and a duration of roughly 40 fs. The spectrum of the probe covers a full-width at half-maximum bandwidth of $\Delta_{BW} = 61$ THz with a center frequency of $f_c = 246$ THz (corresponding to a wavelength of 1.22 μm) supporting a pulse duration of 12 fs with a pulse energy of 0.2 nJ (probe spectra and pulse characterization are given in Supplementary Note 1).

A silicon wafer superimposes both beams on an off-axis parabolic mirror (OAP) focusing them into a gallium selenide (GaSe) or silicon (Si) nonlinear detection crystal (DX). The time delay, t_D, between the pulses is controlled by a variable delay stage (VD). Both pulses are linearly polarized and orthogonal to each other before entering the DX. The polarization change of the probe is then measured with an ellipsometer whose output is read by a lock-in amplifier (at 20 MHz).

In EOS, the interaction between a signal waveform and a broadband probe pulse within a nonlinear crystal is measured versus the variable time delay between them. Based on second-order nonlinearity, the bandwidth of the EOS probe is required to be as large as the carrier frequency of the signal pulse, 156 THz, supporting a pulse duration of order 3 fs[30]. In addition, EOS requires absolute CEP stability of the signal pulse—a constant phase relation between the envelope of the pulse and the underlying oscillations of the field. None of these conditions are fulfilled in our experiment. Nevertheless, when scanning the time delay between the two pulses, few-fs oscillations emerge (see Fig. 2a). The amplitude of the Fourier transform (FT) of the differential current, shown in the inset, reveals a spectral peak centered at 156 THz, i.e., the carrier frequency of our signal (for the spectral phase, see Supplementary Note 2).
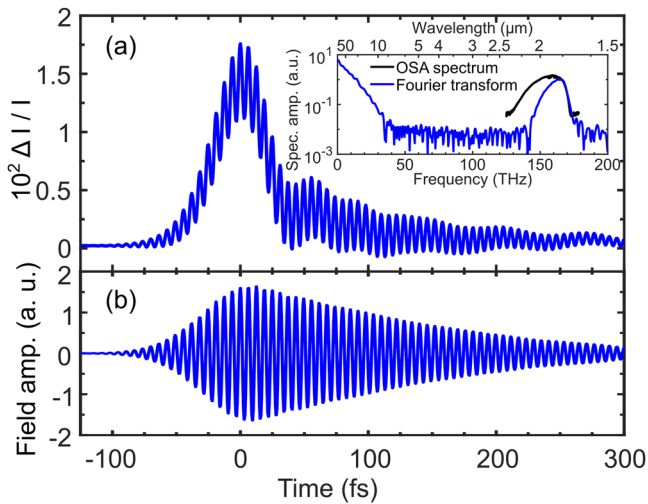
Fig. 2 Time and frequency domain analysis of the output. a Differential photocurrent measured in multi-cycle third-order sampling (MCTOS) as a function of the relative time delay, measured with a 16 μm thick silicon detection crystal in the QWP configuration (see Fig. 1). Inset: Fourier spectrum of the detected signal (blue) plotted on a logarithmic scale versus frequency and compared to the spectral amplitude of the signal pulse, as recorded with an optical spectrum analyzer (OSA, black). **b** The oscillating component of the field extracted from the detected signal in **a** by numerically filtering the Fourier transform (FT) (see inset) around 156 THz and applying the inverse FT.

This observation is surprising for several reasons. Not only are the abovementioned conditions for spectral bandwidth violated, but the signal pulses are not phase stabilized and these oscillations are observed even with a silicon DX whose symmetry precludes a second-order nonlinear interaction. In addition to the rapidly oscillating component, a low-frequency constituent appears in the amplitude of the FT. The physical origin of these results is the focus of the following sections.

Intuitive phasor interpretation. Similar to EOS, the balanced detection scheme employed in MCTOS senses slight variations in the polarization of the probe pulse. These can be described by the generation of new photons through a nonlinear interaction between signal and probe. However, unlike EOS, our results can be explained only by invoking a third-order nonlinearity.

We divide the four-wave mixing interaction into three distinguishable processes that contribute to the MCTOS output. These are depicted in Fig. 3b in a standard arrow scheme; the leftmost arrow is the probe input whereas the fourth arrow from the left stands for the nonlinearly generated probe output. In the first process, referred to as upconversion (UC), a low-frequency probe photon (green arrow) is annihilated and a higher-frequency photon (blue arrow) emerges. Conversely, downconversion (DC) generates an output at a lower frequency. The effective gain and loss of energy in UC and DC, respectively, are represented by black arrows. A third interaction route detected in MCTOS, direct downconversion (DDC), involves two signal photons and was already observed, for example, by Sell et al. [31]. In this case, one signal photon is annihilated and another one is created.

Within a simplified quasi-monochromatic mathematical description, we consider three different angular frequencies for the probe, ω, ω_1, and $\omega + (\Omega - \omega_1)$ along with a single frequency for the signal, Ω. In this case, the complex amplitude of UC and
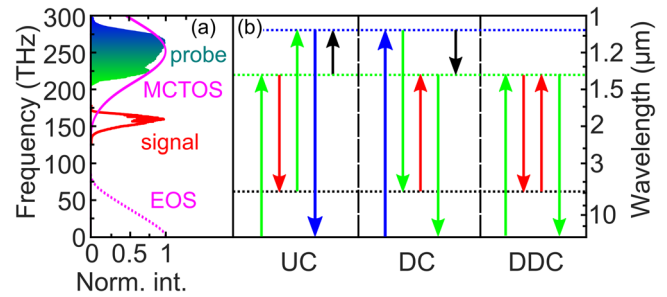

Fig. 3 Third-order nonlinear processes contributing to MCTOS. a Normalized spectral intensities of the probe (turquoise color gradient) and signal (red) pulses. The solid and dashed magenta lines represent the spectral response function of the probe pulse for MCTOS and EOS, respectively. **b** Third-order nonlinear interactions. The length and color of the arrows illustrate the energy of the participating photons. The black arrows represent the effective frequency change of the initial probe photon. UC/DC: up-/downconversion. DDC: direct downconversion.

DDC can be written as

$$
\begin{aligned}
E_{UC}(\omega, t_D) \propto i\chi^{(3)} A_P(\omega_1) A_P\left[\omega + (\Omega - \omega_1)\right] \\
\times A_S(\Omega)\exp\left[i(\Omega t_D + \phi_S - 2\phi_P)\right],
\end{aligned}
\tag{1}
$$

and

$$
E_{DDC}(\omega, t_D) \propto i\chi^{(3)} A_P(\omega)\exp\left[-i\phi_P\right] A_s(\Omega)^2,
\tag{2}
$$

respectively. Here, A_P and A_S represent the real spectral amplitudes of probe and signal, respectively. t_D is the adjustable relative time delay between the pulses and $\chi^{(3)}$ is the third-order nonlinear susceptibility. ϕ_S and ϕ_P are the phases of the signal and probe field, respectively. A full treatment of the broadband case, including all three processes, is given in Supplementary Notes 3–5.

Two significant differences between UC and DDC emerge from these expressions. First, E_{UC} (and E_{DC}) oscillates with respect to t_D at the signal frequency whereas the DDC contribution is a constant. This distinction is clear in Fig. 2a where an oscillating term (UC and DC) is offset by a slowly varying transient (DDC). Since the DDC output is clearly distinguishable from the phase-sensitive contribution in the Fourier domain, it can be readily filtered out (see Methods section). An inverse FT of the filtered output reveals the field transient of the signal pulse (Fig. 2b). Second, and more important for MCTOS, only the UC and DC processes depend on the spectral phases ϕ_S and ϕ_P. As shown below, it is thanks to these interaction paths that MCTOS can directly measure the spectral phase of the signal pulse.

Sensing the fields of these four-wave mixing interactions is accomplished through a homodyne detection scheme. Measuring the interference term between the probe and the newly generated photons, the homodyne output can be conveniently described with a phasor expression - the product of the complex amplitudes of the nonlinear output [Eqs. (1), (2)] and the probe:[30]

$$
\begin{aligned}
P_{UC}(t_D) \propto i\chi^{(3)} A_P(\omega) A_P(\omega_1) A_P\left[\omega + (\Omega - \omega_1)\right] \\
\times A_S(\Omega)\exp\left[i(\Omega t_D + \phi_S - \phi_P)\right],
\end{aligned}
\tag{3}
$$

$$
\begin{aligned}
P_{DC}(t_D) \propto i\chi^{(3)} A_P(\omega) A_P(\omega_1) A_P\left[\omega + (\omega_1 - \Omega)\right] \\
\times A_S(\Omega)\exp\left[-i(\Omega t_D + \phi_S - \phi_P)\right],
\end{aligned}
\tag{4}
$$

$$
P_{DDC}(t_D) \propto i\chi^{(3)} A_P(\omega) A_P(\omega) A_S(\Omega) A_S(\Omega) = i\chi^{(3)}\left|A_P A_S\right|^2.
\tag{5}
$$

Since the polarization of the generated photons is orthogonal to that of the probe, the interference term can be divided into two distinct parts. A field that is in phase with the probe wave results
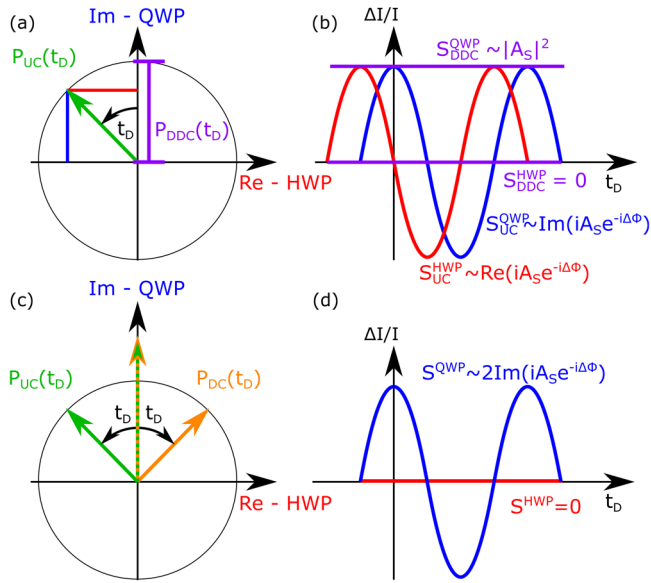
Fig. 4 Phasor representation of the nonlinear interaction processes.
Upper panels: Upconversion (UC) and direct downconversion (DDC)
processes. **a** Green arrow illustrates the phasor of the UC process for a time
delay t_D. The blue and red lines indicate the imaginary and real part of the
phasor and hence the detected output with a quarter- and half-wave plate
(QWP and HWP), respectively. The purple bar represents the phasor of the
DDC process. **b** Corresponding UC and DDC outputs depicted versus
relative time delay with the same color code as in **a**. Lower panels: The sum
of UC and downconversion (DC). **c** Phasors of UC (green arrow) and DC
(orange arrow) and their sum (green-orange dashed arrow). **d** Output of
the sum of UC and DC when detected with a QWP and HWP in blue and
red, respectively. $\Delta\Phi = \Phi_S$-Φ_P: relative phase difference between signal
and probe.

in a rotation of the linear polarization of the probe and
corresponds to the real part of the phasor. In contrast, a
nonlinear field output with a π/2 phase offset leads to an
elliptically polarized interference signal and corresponds to the
imaginary portion of the phasor. A balanced ellipsometer
equipped with a quarter-wave plate (QWP) detects the imaginary
part (π/2-phase-shifted component) of the phasor whereas one
with a half-wave plate (HWP) obtains the real part (in-phase
component)[30].

Fig. 4 depicts the complex phasors (left) and the corresponding
detected waveforms (right) for the three interaction routes
described above [Eqs. (3)-(5)]. Since the DDC phasor is not
oscillating and purely imaginary (vertical purple bar in Fig. 4a),
its output is constant and only measurable with a QWP (Fig. 4b).
With an increasing time delay t_D, the UC phasor (Fig. 4c, green
arrow) rotates anticlockwise in the complex plane with an angular
frequency Ω [Eq. (3)] while the DC phasor (Fig. 4c, orange arrow)
rotates with the same frequency in the opposite direction. The
sum of both phasors (orange-green dashed arrow) constantly
points along the imaginary axis, with a periodically varying
amplitude. As a result, the total signal from DC and UC is also
detectable only in a QWP ellipsometer configuration (Fig. 4d).
Altogether, it is this periodic evolution of the phasor projection
that manifests as the phase sensitive MCTOS signal – an
oscillation with the carrier frequency of the signal (Fig. 2).

Comparison with an analytical model. While the quasi-
monochromatic intuitive phasor picture already explains the
main features of MCTOS, a rigorous mathematical treatment is
required for the case of broadband fields (Supplementary

Notes 3–5). In the following, we quantitatively compare the
broadband modeling to our results.

The summed differential current resulting from the UC and
DC processes and detected by QWP or HWP configuration can
be written as

$$\Delta I^{QWP}(t_D) \propto \int_0^\infty \text{Re}\{[R_{UC}(\Omega) + R_{DC}(\Omega)] \\ \times A_S(\Omega)\exp[-i(\Delta\phi^0 + \phi_S^{ho})]\exp(-i\Omega t_D)\}d\Omega, \quad (6)$$

$$\Delta I^{HWP}(t_D) \propto \int_0^\infty \text{Im}\{[R_{UC}(\Omega) - R_{DC}(\Omega)] \\ \times A_S(\Omega)\exp[-i(\Delta\phi^0 + \phi_S^{ho})]\exp(-i\Omega t_D)\}d\Omega. \quad (7)$$

Since both the signal and the probe are derived from the same
master oscillator, $\Delta\phi^0$, the CEP difference between them, can
be treated as a constant. The higher-order spectral phase of
the signal field is given by $\phi_S^{ho} = \phi_S^{(2)} \cdot (\Omega - \Omega_0)^2 + \phi_S^{(3)} \cdot (\Omega - \Omega_0)^3 + \dots$, where Ω_0 is the central frequency of the
signal. This phase contains the non-trivial information about the
temporal form of the electric field. R_{UC} and R_{DC} are the spectral
response functions for UC and DC, respectively, which depend
on the spectrum of the probe and the phase-matching of the
third-order nonlinear interaction. These expressions confirm the
intuitive picture presented in the previous section: The FT of the
MCTOS output provides a direct measurement of the spectral
amplitude and phase of the signal pulse within the bandwidth
offered by the response functions, see Supplementary Note 6.

The spectral response functions (R_{UC} and R_{DC}) are generally
not identical and as a consequence, a phase-sensitive output is
expected also for the HWP configuration. In particular, a similar
output for the QWP and HWP is obtained when suppressing
either the UC or DC contribution.

To experimentally explore this observation, we detect the
output with a 25 μm thick GaSe DX and spectrally filter the probe
to modify the UC and DC response functions. Essentially,
upconverted photons gain energy and therefore tend to appear in
the higher-frequency part of the probe spectrum. Inserting 50 nm
wide bandpass filters with different center frequencies after the
detection crystal (see Fig. 1) spectrally resolves the detection
process. Figure 5 presents the results of such an experiment: An
MCTOS output for a bandpass filter centered at 286 THz is
shown in Fig. 5a, b, those for a 214 THz central frequency in
Fig. 5c, d and those for 250 THz central frequency in Fig. 5e, f. In
all three rows, the left panel depicts the detected transients for the
QWP (blue) and HWP (red) configurations, while the corre-
sponding amplitudes of their Fourier transform are given on the
right panel.

Applying a BPF centered at the high-frequency edge of the
probe (see inset of Fig. 5b), favors upconverted photons (cf.
Fig. 3b). Consequently, both ellipsometer configurations (QWP
and HWP) measure an oscillating output (Fig. 5a) with nearly
identical spectral components (Fig. 5b). This behavior is also
predicted by the monochromatic picture (Fig. 4a and b). The
numerically calculated spectrum for the UC interaction (green
dashed line) demonstrates a high level of agreement with the
experimental results. Thus, we are able to suppress the effect of
the DC process by spectral filtering. Qualitatively similar results
are obtained for a postselection of downconverted photons,
achieved by filtering around 214 THz (Fig. 5c, d).

In contrast, isolating the central part of the probe spectrum
(around 250 THz) effectively reduces the bandwidth for the
detection of the phase-sensitive output. As a result, the oscillating
transients detected in MCTOS significantly reduce (Fig. 5e) and
their spectra are blue-shifted (Fig. 5f). The finite DDC
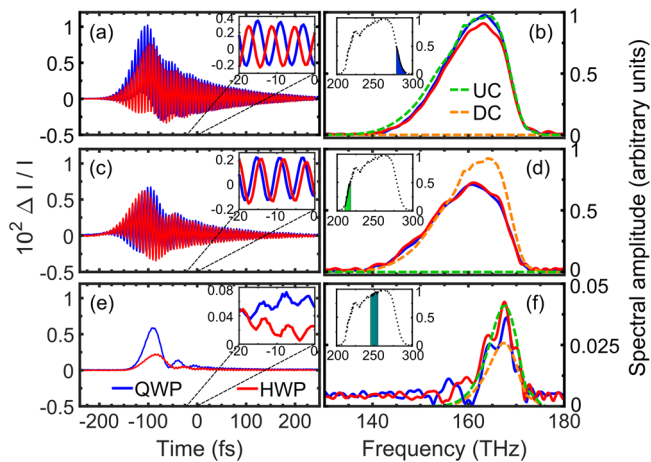contribution to the output of the HWP configuration (Fig. 5e)

Fig. 5 Wavelength-resolved analysis of the MCTOS output.
a, **c**, **e** Differential current versus time delay measured using quarter- (blue) and half-wave plate (red). The insets show a zoomed-in version of the data. **b**, **d**, **f** Corresponding spectral amplitudes with the same color coding as on the left-hand side. The numerical simulations for up- and downconversion are displayed in green and orange dashed lines, respectively. All spectra are normalized to the maximum of the measurement in the QWP configuration in **b**. The insets visualize the normalized probe spectrum (dotted line) with the transmitted spectral range of the bandpass filters (color shaded areas). Measurements were performed with a 25 μm thick GaSe DX.

is likely due to the dispersion of the detection crystal as further discussed in Supplementary Note 5.

We note that using a Si DX provides similar experimental observations, but their analysis and numerical modeling are less straightforward. The spectral overlap of the Si bandgap with the probe pulse results in a more complex dispersion and absorption spectrum that must be considered.

To discuss the spectral response of MCTOS, we first consider that the homodyne scheme is highly sensitive only within the frequency range of the probe. Thus, detection occurs only if the upconverted or downconverted photon spectrally overlaps with the probe.

Consequently, the sensitivity range of MCTOS is $\left[f_c - 3/2\Delta_{BW}, f_c + 3/2\Delta_{BW}\right]$ (full magenta line, Fig. 3a), where f_c and Δ_{BW} are the center frequency and bandwidth of the probe, respectively. In the current setup, this range extends from 155 to 339 THz. The frequency range of MCTOS is thus complementary to EOS whose response vanishes at higher frequencies (dashed magenta line, Fig. 3a).

The bandwidth is noticeable when comparing the spectrum of our first dataset to that obtained with a commercial optical spectrum analyzer (OSA) (black line, inset of Fig. 2a). At frequencies below the sensitivity range of MCTOS, the signal sharply drops with respect to the reference measurement. As the MCTOS transient is simply a Fourier transform of the complex-valued spectrum, such spectral narrowing manifests as temporal stretching of the oscillating component (Fig. 2b) with respect to the original signal pulse.

A second indication for the role of the response function, $R(\Omega)$, is observed in Fig. 5. Applying a spectral filter at either edge of the probe spectrum broadens the response function of MCTOS in the frequency domain, as thoroughly discussed in Supplementary Note 6. Filtering in detection can also simplify MCTOS in the case of spectral overlap between the signal and the probe. A filter excluding the signal pulse spectrum suppresses the linear interference term between the signal and probe pulses, which may otherwise obscure the MCTOS output. As such, an optimal choice for detection filter rejects the signal spectrum while
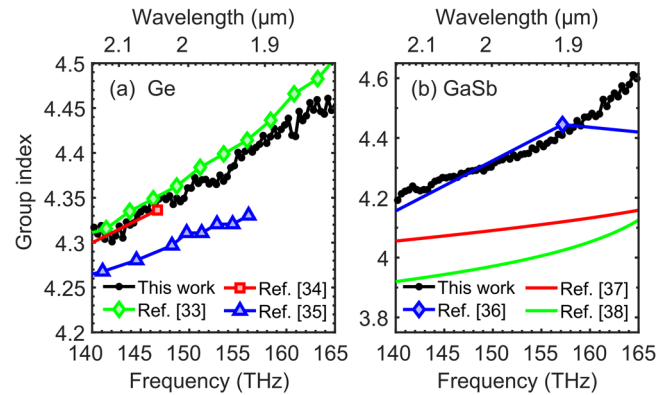

Fig. 6 Applying MCTOS to obtain the group index of refraction. Group-index measurements of **a** germanium (Ge) and **b** gallium antimonide (GaSb) samples. Our results (black circles) are compared with several references (colored, see legend). Data points are depicted as markers while the lines are a guide to the eye. Since Refs. [37,38]. are parameterizations, only a solid line is depicted.

transmitting only a fraction of the probe in either its high- or low-energy edge.

Another factor that impacts the MCTOS response function is the spectral phase of the probe pulse. Naturally, an optimal bandwidth is obtained for a transform-limited probe pulse while significant chirping results in spectral narrowing, as described in detail in Supplementary Note 6. In the current experiment, we synthesize a transform-limited probe pulse, as indicated by the results of a frequency-resolved-optical-gating (FROG) measurement (see Supplementary Note 1). Finally, we note that beyond the bandwidth covered by the current experimental implementation, a significant advantage of MCTOS, in comparison with EOS, is its tunability. The central frequency of the probe branch can be readily tailored to cover a specific spectral region through nonlinear interactions in fiber[29] or free-space[32] optics.

Application—group index dispersions. Having confirmed our conceptual and theoretical considerations in the previous sections, we now exploit our quantitative understanding of MCTOS to present its first application: characterizing the phase response of two important optical materials in the MIR. Specifically, we measure the dispersion of the group index of refraction by recording the transients of the signal pulse with and without a specimen.

The group index $n_g(\Omega)$ is readily extracted from the difference of the spectral phases between the two measurements $\Delta\phi(\Omega)$ (see Supplementary Note 7) according to

$$n_g(\Omega) = 1 + \frac{c}{d}\frac{\partial\Delta\phi(\Omega)}{\partial\Omega},\qquad(8)$$

where c is the speed of light and d is the thickness of the specimen.

The extracted dispersion of the group index for germanium (Ge) and gallium antimonide (GaSb) are depicted in black circles in Fig. 6a, b, respectively. The results for Ge show an excellent agreement with published experimental data[33–35] in the entire spectral range covered while providing a much higher spectral resolution. This confirms the phase-sensitivity of MCTOS as well as its high reliability for spectral phase measurement.

For GaSb (Fig. 6b), experimental data is scarce[36] and only two publications[37,38] modeling absorption in the spectral region of interest are available. While a reasonable agreement is obtained

with the sparse experimental data, our measurements strongly deviate from the results of both numerical modeling works.

The use of Ge in high-speed electronic components[39] and the potential application of GaSb for next-generation high-electron-mobility transistors (HEMTs)[40] demonstrate the importance of these fundamental semiconductors. Therefore, the sparsity of MIR refractive index measurements, close to the bandgap, is another indication of the lack of a simplified experimental approach for phase-sensitive detection in this spectral region.

Conclusion

In summary, we present here MCTOS—a technique for measuring the spectral phase and amplitude of infrared electric-field transients. The pump-probe scheme, relying on third-order nonlinear interaction, circumvents the requirement for an ultrashort gating pulse altogether. A thorough experimental and theoretical analysis reveals that the detected polarization change of the probe pulses can be understood in the frequency domain as up- and downconversion of near-infrared probe photons similar to the case of EOS. As a proof-of-principle demonstration, we measured the dispersion of the group index of Ge and GaSb.

Unlike conventional EOS suited for low THz frequencies, the sensitivity spectrum of MCTOS is dictated by the center frequency of the probe and can therefore be tailored to fit the spectral content of the signal. Altogether, MCTOS is an excellent candidate to simplify temporally and spatially resolved measurements of the full dielectric function (real and imaginary) in a broad spectral range. As such it may also become valuable for spectroscopic studies of electronic and vibrational transient states, for example, in chemistry and solid-state physics.

Methods

Laser source and optical setup. In this work, we employ a custom-built laser system. The laser oscillator is entirely fiber-based and relies on polarization maintaining optical components. Erbium-doped fibers act as an active gain medium and a pigtail saturable absorber mirror (BATOP; SAM-1550-33-2ps) enables stable and self-starting mode-locking. A pulse-picking EOM (Jenoptik; AM1550) based on $LiNbO_3$ reduces the repetition rate of the signal branch prior to pulse amplification. The output of the oscillator is split and input into two self-constructed erbium-doped fiber amplifiers (EDFA) that are based solely on fiber components, as well.

Each amplified pulse is coupled into a highly nonlinear fiber, optimized to generate a broadband dispersive wave and a low-frequency soliton for the probe and signal pulse, respectively[41]. For each branch, fine-tuning of the output spectra is achieved with a silicon-prism compressor before the pulse enters the HNF. The signal-branch pulse is spectrally filtered with a 150 μm thick gallium antimonide wafer set at Brewster's angle. The filter's second-order dispersion is compensated for with fused silica windows. The probe branch pulse is temporally compressed with a pair of SF10 glass prisms. Inserting a razor blade in the Fourier plane of the prism pair acts as a spectral filter.

The two branches overlap in a nonlinear crystal (25 μm thick GaSe or 16 μm thick Si) where third-order nonlinear interactions occur. The GaSe detection crystal is physically exfoliated from a bulk sample, whereas the Si crystal is polished out of a thicker wafer. The output of the nonlinear interaction in the crystal is measured by an ellipsometer setup based on a commercially available balanced photodiodes module (PDB440C, Thorlabs) with two InGaAs detectors. The balanced signal is read out by a radio-frequency lock-in amplifier (UHF, Zurich Instruments) with a 20 MHz reference frequency input.

To filter out the DDC contribution (see Fig. 2), first, a FT of the detected output calculates the spectral amplitude and phase (inset of Fig. 2a). Thanks to their large frequency difference, the DDC contribution (0 to 40 THz) can be separated from the field-sensitive components—UC and DC (140–170 THz). To do so, we multiply the spectral amplitude with a super-Gaussian function, $\exp\left[-\left(\frac{f-f_0}{\Delta f}\right)^6\right]$, with $f_0 = 155$ THz and $\Delta f = 80$ THz. An inverse FT of the filtered high-frequency component (Fig. 2b) extracts the electric-field transient of the signal.

Data availability

Data underlying the results and its analysis script may be obtained from the authors upon reasonable request.

References

1. Tamming, R. R. et al. Ultrafast spectrally resolved photoinduced complex refractive index changes in CsPbBr 3 perovskites. *ACS Photonics* **6**, 345–350 (2019).
2. Tokunaga, E., Terasakiy, A. & Kobayashi, T. Femtosecond phase spectroscopy by use of frequency-domain interference. *J. Opt. Soc. Am. B* **12**, 753 (1995).
3. Tanghe, I. et al. Broadband optical phase modulation by colloidal CdSe quantum Wells. *Nano Lett.* **22**, 58–64 (2022).
4. Tokunaga, E., Kobayashi, T. & Terasaki, A. Frequency-domain interferometer for femtosecond time-resolved phase spectroscopy. *Opt. Lett.* **17**, 1131 (1992).
5. Bionta, M. R. et al. On-chip sampling of optical fields with attosecond resolution. *Nat. Photonics* **15**, 456–460 (2021).
6. Kim, K. T. et al. Petahertz optical oscilloscope. *Nat. Photonics* **7**, 958–962 (2013).
7. Dam, J. S., Tidemand-Lichtenberg, P. & Pedersen, C. Room-temperature mid-infrared single-photon spectral imaging. *Nat. Photonics* **6**, 788–793 (2012).
8. Gordon, R. Room-temperature mid-infrared detectors. *Science* **374**, 1201–1202 (2021).
9. Zhang, X.-C. & Xu, J. *Introduction to THz Wave Photonics*. (Springer US, 2010).
10. Burford, N. M. & El-Shenawee, M. O. Review of terahertz photoconductive antenna technology. *Opt. Eng.* **56**, 010901 (2017).
11. Wu, Q. & Zhang, X. C. Free-space electro-optic sampling of terahertz beams. *Appl. Phys. Lett.* **67**, 3523 (1995).
12. Kübler, C., Huber, R., Tübel, S. & Leitenstorfer, A. Ultrabroadband detection of multi-terahertz field transients with GaSe electro-optic sensors: approaching the near infrared. *Appl. Phys. Lett.* **85**, 3360–3362 (2004).
13. Tidemand-Lichtenberg, P., Dam, J. S., Andersen, H. V., Høgstedt, L. & Pedersen, C. Mid-infrared upconversion spectroscopy. *J. Opt. Soc. Am. B* **33**, D28 (2016).
14. Huang, K., Fang, J., Yan, M., Wu, E. & Zeng, H. Wide-field mid-infrared single-photon upconversion imaging. *Nat. Commun.* **13**, 1077 (2022).
15. Kono, S., Tani, M., Gu, P. & Sakai, K. Detection of up to 20 THz with a low-temperature-grown GaAs photoconductive antenna gated with 15 fs light pulses. *Appl. Phys. Lett.* **77**, 4104–4106 (2000).
16. Keiber, S. et al. Electro-optic sampling of near-infrared waveforms. *Nat. Photonics* **10**, 159–162 (2016).
17. Park, S. B. et al. Direct sampling of a light wave in air. *Optica* **5**, 402 (2018).
18. Liu, Y., Beetar, J. E., Nesper, J., Gholam-Mirzaei, S. & Chini, M. Single-shot measurement of few-cycle optical waveforms on a chip. *Nat. Photonics* **16**, 109–112 (2022).
19. Herbst, A. et al. Recent advances in petahertz electric field sampling. *J. Phys. B At. Mol. Opt. Phys.* **55**, 172001 (2022).
20. Ludwig, M. et al. Sub-femtosecond electron transport in a nanoscale gap. *Nat. Phys.* **16**, 341–345 (2020).
21. Krüger, M., Schenk, M. & Hommelhoff, P. Attosecond control of electrons emitted from a nanoscale metal tip. *Nature* **475**, 78–81 (2011).
22. Herink, G., Solli, D. R., Gulde, M. & Ropers, C. Field-driven photoemission from nanostructures quenches the quiver motion. *Nature* **483**, 190–193 (2012).
23. Schiffrin, A. et al. Optical-field-induced current in dielectrics. *Nature* **493**, 70–74 (2013).
24. Rybka, T. et al. Sub-cycle optical phase control of nanotunnelling in the single-electron regime. *Nat. Photonics* **10**, 667–671 (2016).
25. Pupeza, I. et al. Field-resolved infrared spectroscopy of biological systems. *Nature* **577**, 52–59 (2020).
26. Liu, Y. et al. All-optical sampling of few-cycle infrared pulses using tunneling in a solid. *Photonics Res.* **9**, 929 (2021).
27. Wyatt, A. S. et al. Attosecond sampling of arbitrary optical waveforms. *Optica* **3**, 303 (2016).
28. Hammond, T. et al. Near-field imaging for single-shot waveform measurements. *J. Phys. B . Mol. Opt. Phys.* **51**, 065603 (2018).
29. Brida, D., Krauss, G., Sell, A. & Leitenstorfer, A. Ultrabroadband Er:fiber lasers. *Laser Photon. Rev.* **8**, 409–428 (2014).
30. Sulzer, P. et al. Determination of the electric field and its Hilbert transform in femtosecond electro-optic sampling. *Phys. Rev. A* **101**, 033821 (2020).
31. Sell, A., Leitenstorfer, A. & Huber, R. Phase-locked generation and field-resolved detection of widely tunable terahertz pulses with amplitudes exceeding 100 MV/cm. *Opt. Lett.* **33**, 2767 (2008).
32. Cerullo, G. & De Silvestri, S. Ultrafast optical parametric amplifiers. *Rev. Sci. Instrum.* **74**, 1–18 (2003).

33. Nunley, T. N. et al. Optical constants of germanium and thermally grown germanium dioxide from 0.5 to 6.6 eV via a multisample ellipsometry investigation. *J. Vac. Sci. Technol. B* **34**, 061205 (2016).

34. Burnett, J. H., Benck, E. C., Kaplan, S. G., Stover, E. & Phenis, A. Index of refraction of germanium. *Appl. Opt.* **59**, 3985 (2020).

35. Li, H. H. Refractive index of silicon and germanium and its wavelength and temperature derivatives. *J. Phys. Chem. Ref. Data* **9**, 561–658 (1980).

36. Ferrini, R., Patrini, M. & Franchi, S. Optical functions from 0.02 to 6 eV of $Al_xGa_{1-x}Sb/GaSb$ epitaxial layers. *J. Appl. Phys.* **84**, 4517–4524 (1998).

37. Djurišić, A. B., Li, E. H., Rakić, D. & Majewski, M. L. Modeling the optical properties of AlSb, GaSb, and InSb. *Appl. Phys. A Mater. Sci. Process.* **70**, 29–32 (2000).

38. Adachi, S. Optical dispersion relations for GaP, GaAs, GaSb, InP, InAs, InSb, $Al_xGa_{1-x}As$, and $In_{1-x}Ga_xAs_yP_{1-y}$. *J. Appl. Phys.* **66**, 6030–6040 (1989).

39. Washio, K. SiGe HBT and BiCMOS technologies for optical transmission and wireless communication systems. *IEEE Trans. Electron Devices* **50**, 656–668 (2003).

40. Bennett, B. R., Magno, R., Boos, J. B., Kruppa, W. & Ancona, M. G. Antimonide-based compound semiconductors for electronic devices: a review. *Solid. State Electron.* **49**, 1875–1895 (2005).

41. Sell, A., Krauss, G., Lohss, S., Huber, R. & Leitenstorfer, A. 8-fs pulses from a compact Er: fiber laser system. *Opt. Express* **17**, 287–291 (2009).

Author contributions

A.Le. initiated the study and supervised its progress. H.K and A.Le. posed the original scientific question. H.K. designed the experimental setup with support from P.S. and A.Li. H.K. performed the optical experiments and the simulations. R.T. and H.K. analyzed the data, refined the physical understanding, and prepared the manuscript with significant contributions from all authors.

Competing interests

The authors declare no competing interests.

Additional information

Supplementary information The online version contains supplementary material available at https://doi.org/10.1038/s42005-023-01269-y.

Correspondence and requests for materials should be addressed to Ron Tenne.

Peer review information *Communications Physics* thanks Brian Julsgaard and the other, anonymous, reviewer(s) for their contribution to the peer review of this work. A peer review file is available.

Reprints and permission information is available at http://www.nature.com/reprints

Publisher's note Springer Nature remains neutral with regard to jurisdictional claims in published maps and institutional affiliations.